J. Sens. Sens. Syst., 6, 107–119, 2017
www.j-sens-sens-syst.net/6/107/2017/
doi:10.5194/jsss-6-107-2017


JSSS Journal of Sensors and Sensor Systems Open Access

# Oxygen transport in epitaxial $SrTiO_3/SrTi_{1-x}Fe_xO_3$ multilayer stacks

**Michal Schulz[1], Timna Orland[2], Alexander Mehlmann[2], Avner Rothschild[2], and Holger Fritze[1]**

[1]Institute of Energy Research and Physical Technologies, Clausthal University of Technology, Goslar, Germany
[2]Department of Materials Science and Engineering, Technion, Israel Institute of Technology, Haifa, Israel

*Correspondence to:* Michal Schulz (michal.schulz@tu-clausthal.de)

Received: 10 June 2016 – Revised: 13 January 2017 – Accepted: 4 February 2017 – Published: 28 February 2017

**Abstract.** Nano-ionic materials made of strontium titanate ($SrTiO_3$, STO) and solid solutions of strontium ferrite in STO ($SrTi_{1-x}Fe_xO_3$, STF) are grown on single crystalline STO substrates and characterized. Since STF exhibits an oxygen deficiency and, simultaneously, enables oxygen interstitial defects, a space charge area close to the STO | STF interface is present. Oxygen tracer diffusion experiments and impedance spectroscopy at temperatures from 500 to 700 °C and at oxygen partial pressure ranging from $10^{-3}$ to $10^{-23}$ bar confirm fast oxygen transport caused by enhanced ionic conductivity at the interface. There, an oxygen diffusion coefficient of $3.4 \times 10^{-10}$ m$^2$ s$^{-1}$ at 600 °C and a $p$ type conductivity of about 360 S m$^{-1}$ at 700 °C are calculated. Such structures open new options in design of nano-ionic materials for oxygen sensors and energy conversion at temperatures lower than those of conventional materials such as yttrium-doped zirconia.

## 1 Introduction

Increasing worldwide concerns about environmental degradation, global warming, and the need for new renewable energy sources and safety issues regarding, e.g., nuclear power lead to a search for new materials for sensor, energy conversion, and storage applications. Currently used materials such as yttrium stabilized zirconia (YSZ) yield an outstanding performance such as fast ionic transport (Ioffe et al., 1978; Badwal, 1992; Kilo et al., 2004; Gerstl et al., 2011), but require high operating temperatures of at least 700 °C. This situation stimulates growing interest in nano-sized ionic materials which could, for example, reduce the operating temperatures of such devices to economically viable temperatures of about 500 °C. Lowering the temperature and enhancing ionic conductivity lead to systems with, e.g., shorter startup times, shorter response times, reduced heat dissipation, lower internal resistance of the cells, as well as prolonged lifetimes. Such nano-sized ionic systems, however, remain in the early stages of research and development largely because of material limitations. Improved understanding and control of the interfacial ionic transport and innovative means to tailor their ionic conductivity are required to facilitate further development.

This work focuses on investigation of nano-ionic structures comprising alternating layers of metal oxides with oxygen deficiency and excess. Consequently, an increase in concentrations of mobile defects in the form of oxygen vacancies and interstitials and thus enhanced ionic conductivity is expected. The Debye screening length at the interface of nano-ionic layers should be on the order of several tens of nanometers resulting in effects on the oxygen transport visible by oxygen exchange experiments and impedance spectroscopy.

The transport properties in these materials are investigated using oxygen exchange experiments and impedance spectroscopy as a function of temperature and of oxygen partial pressure. The material systems selected for this work are strontium titanate ($SrTiO_3$, STO) and solid solutions of strontium ferrite (SFO) in STO ($SrTi_{1-x}Fe_xO_3$, STF) with 20 (STF20) and 50 mol % SFO (STF50). Diffusion barriers are made of thin lanthanum aluminate ($LaAlO_3$, LAO) and gold layers.

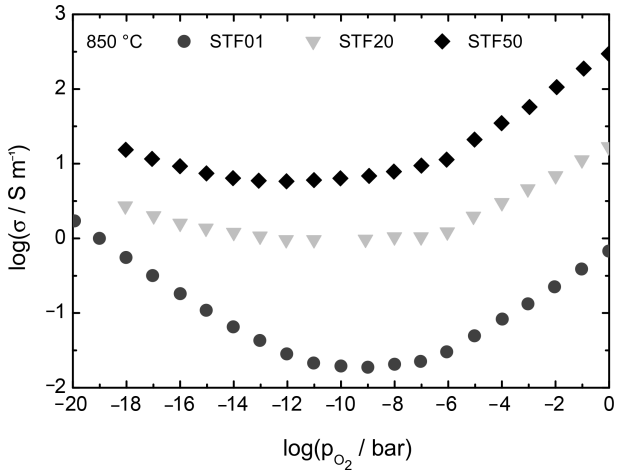


**Figure 1.** Total conductivity of different STF compositions at 850 °C as a function of oxygen partial pressure. Selected data points taken from Heilig (1996).

## 2 Models

### 2.1 Space charge at the interface

STO single crystals show a perovskite structure with a closely packed anion sublattice. Because of size constraints, strontium titanate cannot accommodate interstitial defects $O_i''$. In contrast, it tolerates oxygen vacancies $V_O^{\bullet\bullet}$. STF solid solutions show a double perovskite structure with inherent oxygen deficiency (brownmillerite structure of SFO) which provides sufficient room for oxygen interstitials. The conductivity of STF and STO bulk materials has been investigated previously. For further discussion, an exemplary plot of total conductivity as a function of oxygen partial pressure and STF composition at 850 °C is shown in Fig. 1 (Heilig, 1996).

The stoichiometric composition of STF solid solutions is defined as $SrTi_{1-x}^{+4}Fe_x^{+3}O_{3-x/2}$, where neither Fe nor Ti is regarded as a defect species for Fe concentrations above 1 % (Rothschild, 2006). The preferred oxidation state of Fe is +3, resulting in an inherently oxygen-deficient crystal structure, i.e., in structural oxygen vacancies. Here, the intrinsic disorder is considered to be anion Frenkel defects where oxygen vacancies and interstitials are thermally generated as follows (Rothschild, 2006; Kuhn et al., 2013):

$$O_O + V_i^{\times} \leftrightharpoons O_i'' + V_O^{\bullet\bullet}. \tag{R1}$$

The difference in the standard chemical potential of $V_O^{\bullet\bullet}$ defects enables its transfer from STF through the interface into the STO layer. The increased vacancy concentrations at the interface impact the oxygen transport significantly since the oxygen tracer diffusion coefficient is correlated with the vacancy diffusion coefficient $D_V$ through

$$D_O = f^* D_V \frac{c_{V_O^{\bullet\bullet}}(x)}{c_{O_O^{\times}}(x)}, \tag{1}$$

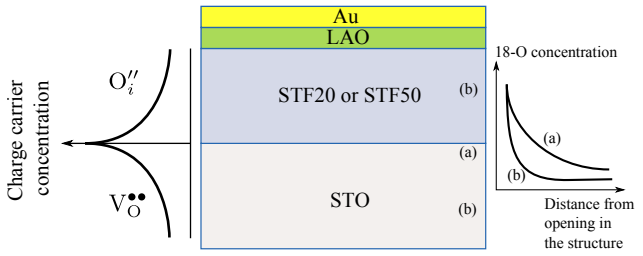


**Figure 2.** Schematic illustration of an interface between STF layer and STO. The oxygen depth profiles along the interface are expected to be much broader close to the interface (a) than in bulk STO or STF (b).

where $c_{V_O^{\bullet\bullet}}(x)$, $c_{O_O^{\times}}(x)$ and $f^*$ are concentrations of oxygen vacancies and oxygen as well as the tracer correlation correction factor, respectively. In the case of an oxygen tracer, the correlation factor is very close to unity and therefore set to unity in further discussion. Since the bulk oxygen concentration, $c_{O_O^{\times}}$, can be assumed to be nearly constant, the diffusion coefficient of oxygen is proportional to the concentration of the vacancies. Therefore, the enhanced space charge close to the interface as depicted in Fig. 2 is expected to facilitate fast oxygen transport in that region. This effect can be controlled by the concentration of a ferrite phase in STF. It can be further increased by creating stacks of interleaved STF and STO layers and adjusting the thicknesses of the structures so that the space charge regions overlap.

### 2.2 Ionic transport

STO is a perovskite structure with well-studied electrochemical properties (e.g., Balachandran and Eror, 1981; Chan et al., 1981; Wagner et al., 2004; De Souza, 2009; Ohly et al., 2006; Gömann et al., 2005, 2004). The oxygen partial pressure dependence of its mixed ionic–electronic conductivity makes it a good candidate for high temperature gas sensor applications (Fergus, 2007; Hu et al., 2004). Depending on the oxygen partial pressure, three regions with different $p_{O_2}$ dependence may be regarded (Steinsvik et al., 1996; De Souza, 2009, 2015; Shi, 2016).

#### 2.2.1 Low oxygen partial pressures

At low oxygen partial pressures, oxygen atoms tend to leave the crystal lattice, generating oxygen vacancies and free electrons compensating the charge

$$O_O^{\times} \leftrightharpoons V_O^{\bullet\bullet} + \frac{1}{2}O_2 + 2e' \tag{R2}$$

with the equilibrium

$$K_{Red}(T) = p_{O_2}^{\frac{1}{2}} n^2 \left[V_O^{\bullet\bullet}\right]. \tag{2}$$

As long as the concentration of oxygen vacancies formed by unintended acceptor doping and/or Frenkel defects exceeds

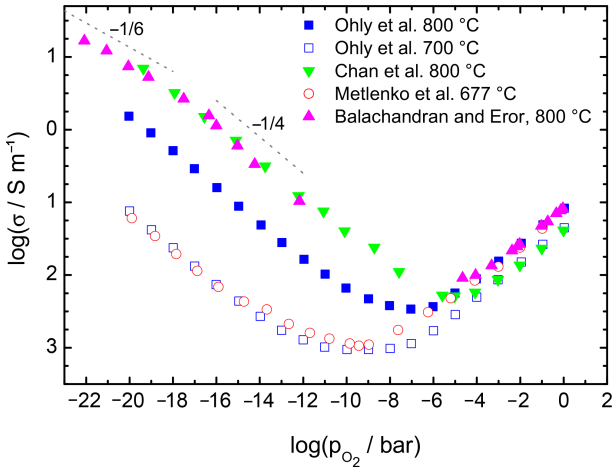


**Figure 3.** Total conductivity in STO as a function of oxygen partial pressure and temperature as reported by several authors (Ohly et al., 2006; Chan et al., 1981; Balachandran and Eror, 1981; Metlenko et al., 2014).

the number of vacancies generated due to reduction of STO significantly, $[V_O^{\bullet\bullet}]$ is approximately constant. Therefore, the $n$ type electronic conductivity depends on the oxygen partial pressure $p_{O_2}$ according to

$$\sigma_n \propto p_{O_2}^{-\frac{1}{4}}. \tag{3}$$

Further reduction of STO at even lower oxygen partial pressure and/or higher temperature (see Fig. 3) may generate a sufficiently large number of oxygen vacancies to make the approximation $[V_O^{\bullet\bullet}] = \text{const}$ invalid. There, the $p_{O_2}$ dependence of $n$ type electronic conductivity changes to

$$\sigma_n \propto p_{O_2}^{-\frac{1}{6}}. \tag{4}$$

### 2.2.2 Intermediate oxygen partial pressures

At intermediate oxygen partial pressures the ionic conductivity dominates, with oxygen vacancies being the prevalent mobile charge carriers.

$$\sigma_{\text{ion}} = \frac{4q^2}{kT}\left[O_O^{\times}\right] D_O \tag{5}$$

### 2.2.3 High oxygen partial pressures

At high oxygen partial pressures the oxygen atoms fill the structural vacancies. As a result of this reaction holes are generated to compensate the charge,

$$V_O^{\bullet\bullet} + \frac{1}{2}O_2 \leftrightharpoons O_O^{\times} + 2h^{\bullet} \tag{R3}$$

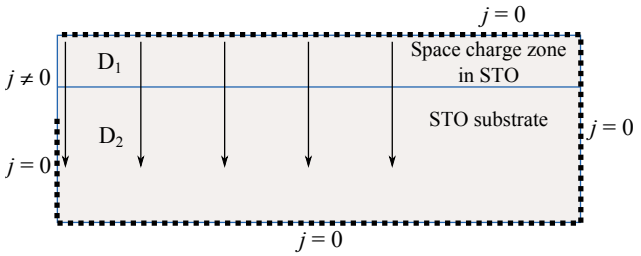


**Figure 4.** Diffusion model (not to scale) used to simulate the 2-D diffusion process through the space charge zone of STO and crystal bulk. The dotted line covering most of the outer boundaries represents an area with zero flow; the arrows inside the area represent places where depth profiles are acquired (see below).

with the equilibrium

$$K_{\text{Ox}}(T) = p_{O_2}^{-\frac{1}{2}} p^2 \left[V_O^{\bullet\bullet}\right]^{-1}. \tag{6}$$

The concentration change in oxygen atoms at oxygen crystal sites is negligible and may be regarded as constant. Therefore, the $p$ type electronic conductivity depends on the $p_{O_2}$ as follows:

$$\sigma_p \propto p_{O_2}^{\frac{1}{4}}. \tag{7}$$

The total conductivity of STO, $\sigma_{\text{tot}} = \sigma_n + \sigma_{\text{ion}} + \sigma_p$, as reported by several authors is summarized in Fig. 3.

### 2.2.4 Impact of space charge zone on the conductivity

As mentioned above, thermally generated anion Frenkel defects in STF cause an enhanced concentration of charge carriers in the vicinity of the interface, i.e., oxygen interstitials $O_i''$ in STF and oxygen vacancies $V_O^{\bullet\bullet}$ in STO. Since STF exhibits a disordered perovskite structure, the oxygen defects are assumed to be mobile and thus contribute to ionic conductivity, as is reported in the case of SFO when it switches from brownmillerite to disordered perovskite by increasing the oxygen partial pressure (Kozhevnikov et al., 2001). At low oxygen partial pressures Reaction (R2) takes place. As long as the oxygen partial pressure is not extremely low, the oxygen vacancy concentration is nearly fixed due to the oxygen vacancies already present in the lattice. Thus the $n$ type electronic conductivity follows the $p_{O_2}$ dependence given by Eq. (3). At high oxygen partial pressures the oxygen may occupy the oxygen vacancies (Reaction R3) and thus provide a significant number of holes contributing to the $p$ type conductivity. Finally, at intermediate oxygen partial pressure the electronic conduction by holes and electrons is low and the ionic conduction through oxygen vacancies is visible.

Since the thickness of the space charge zone is several orders of magnitude lower than the sum of thicknesses of all other components of the sample, its measurable impact on the conductivity is expected to be relatively low. The increase

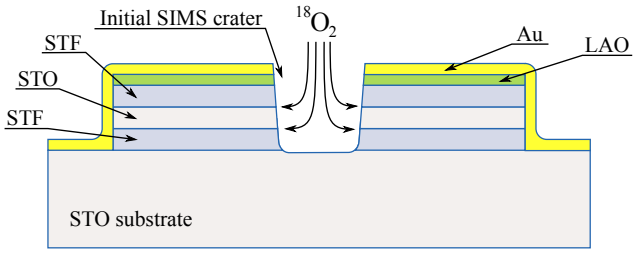


**Figure 5.** A scheme of a sample with two STF layers and an STO layer deposited on the substrate as well as the initial SIMS crater for oxygen access.

in $n$ type conductivity at low $p_{O_2}$ or $p$ type conductivity at high $p_{O_2}$ depends on the equilibrium of the Reactions (R2) and (R3), respectively. These in turn can be correlated with TGA measurements. In the case of STF samples investigated by Kuhn et al. (2013), filling of oxygen vacancies at high oxygen partial pressures is more likely ($\delta = 0.08$ at $p_{O_2} = 10^{-1}$ bar) than oxygen removal at low $p_{O_2}$ ($\delta = -0.01$ at $p_{O_2} = 10^{-27}$ bar). This explains the asymmetry in the behavior of $p$ and $n$ type conductivity in the material.

#### 2.2.5 Modeling of oxygen transport along the interface

In order to estimate the influence of the space charge layer on the overall oxygen transport and, in turn, on the oxygen partial pressure-dependent conductivity, a 2-D model of the interface, including the STO substrate, is created. The model shown in Fig. 4 has the following constraints.

- The oxygen flow from outside into the sample occurs in a small section at the left border of the model area only. In practice, the oxygen access is enabled by an initial crater crated by ion etching as depicted in Fig. 5. This section is deep enough to cover both the space charge zone in STO as well as a 10 to 20 nm deep portion of the STO substrate. Apart from that section, the oxygen flow is set to zero ($j = 0$).

- The oxygen diffusion coefficients in the STO space charge zone and in the STO substrate equal $D_1$ and $D_2$, respectively.

- The thickness of the space charge zone is chosen to be 30 nm. The thickness of the STO substrate is about 1 µm, which is sufficiently high to enable diffusion into a virtually semi-infinite space.

The oxygen diffusion in the model described above is simulated using Comsol Multiphysics software (Comsol, 2016).

Results of the simulation are subsequently compared with experimental results. Here, cross sections and line scans (denoted by vertical arrows in Fig. 4) are analyzed. As explained in Sect. 4.3.3, the simulation provides the lower limit for the diffusion coefficient only.

## 3 Experimental

A scheme of a layer sequence deposited on a STO substrate is shown in Fig. 5. The sample is covered with a LAO | Au diffusion barrier to prevent unintended oxygen access. The opening for oxygen transport into the structure is etched into the barrier and the structure underneath using an Ar ion source. A focused ion beam allows one to precisely control the shape of the crater. Since the primary beam of a SIMS instrument is used, the depth-dependent distribution of elements such as the Sr, Ti, O and Fe of the as-prepared samples is determined simultaneously. After annealing in $^{18}O_2$-enriched gas, SIMS analysis is done in a larger area around the initial crater in order to calculate the 3-D distribution of $^{18}O$ in the form of the ratio $[^{18}O] / ([^{16}O] + [^{18}O])$. Thereby, square brackets represent the concentration of the elements with respect to the chemical formula of the respective compound. If required, the SIMS counts are normalized based on sample sections with known concentrations. In the case of different isotopes of the same element, the ratio of the concentrations follows directly the ratio of the SIMS counts due to identical ionization probabilities.

### 3.1 Sample preparation

All layers are synthesized on a (100) face of single crystalline $10 \times 10 \times 0.5\,mm^3$ $SrTiO_3$ substrates. The STO samples are masked in order to limit the deposited area to approximately $7 \times 7\,mm^2$ and are installed in a vacuum chamber. Subsequently the samples are heated up to approximately 700 °C. Later, thin layers of target materials are epitaxially grown on the STO surface by means of pulsed laser deposition (PLD) using a KrF excimer laser. Depending on the requested arrangement either STF50 or STF20 or alternating layers of STF and STO with a thickness of 50 or 100 nm are deposited. Finally, a 20 nm LAO layer is provided to prevent oxygen diffusion. For further improvement of the oxygen barrier, samples to be used for oxygen diffusion experiments are coated with a thin Au layer using a Cressington Sputter Coater 108.

### 3.2 Oxygen-18 tracer diffusion

The diffusion path for oxygen is opened by initial SIMS analysis. Thereby a rectangular crater of approximately $500 \times 750\,\mu m^2$ is created in the middle of the sample. The measurements provide information about oxygen isotope abundance, arrangement of the deposited layers and interfaces in the as-prepared samples.

The diffusion runs in $^{18}O_2$-enriched gas are performed in a furnace with a transfer rod which enables quick insertion or removal of the sample into or from the hot area. Prior to the diffusion runs each sample is pre-annealed in $^{16}O_2$ at the temperature chosen for the subsequent annealing in $^{18}O_2$ to enable oxygen equilibration throughout the area of interest.

The process is performed at the same oxygen partial pressure, but the annealing time is increased by a factor of 4 at least.

After pre-annealing, the samples are quickly removed from the hot zone of the furnace and the atmosphere is replaced by a $^{18}O_2$-enriched gas (concentration > 85 %). Subsequently, the samples are transferred again into the hot zone and annealed. Finally, the samples are removed from the furnace and cooled down quickly.

The diffusion runs are performed at temperatures from 500 up to 700 °C. Higher temperatures are out of the scope of this work.

### 3.3 Oxygen transport

The SIMS measurements are performed with a Hiden Analytical SIMS Workstation. Here, a primary $Ar^+$ ion beam with a spot diameter of approximately 80 µm is used. The Ar ions are accelerated in a 5 kV field; the intensity of the primary ion beam is set to 100 nA. The analyzed surface area for depth profiles is $500 \times 750\,\mu m^2$. Disturbances of the measurement from crater walls are reduced by gating the acquisition area electronically to about $100 \times 100\,\mu m^2$. In order to reduce the impact of surface charging during the sputter process, an electron flood gun with energy set to 10 eV is used.

After diffusion runs the samples are analyzed for the second time using the scanning mode of the SIMS system. Here, a larger area of $2.1 \times 1.6\,mm^2$ is analyzed. The signals from the quadrupole mass spectrometer for $^{16}O^-$ and $^{18}O^-$ are recorded for every beam position on the sample. Using this technique a 3-D profile of the relative $^{18}O$ concentration through the deposited layers down to the STO substrate is created.

### 3.4 Electrical conductivity

To determine the electrical impedance, STF20 | STO rods with dimensions of $10 \times 2 \times 0.5\,mm^2$ are cut. Subsequently, Pt paste is applied at the ends of the rod on the side where STF20 is present, and two platinum wires are attached to it. Further, the sample is sintered for a short time at 1000 °C. A SIMS analysis of the rod at the end of the experiments confirms that the layered structure is not damaged due to the diffusion of iron during the sintering process. Finally, the samples are installed in a gas-tight tube furnace which is equipped with an oxygen ion pump and in-house designed control electronics to adjust the oxygen partial pressure in a range from $10^{-3}$ to $10^{-23}$ bar (Schulz et al., 2012).

The samples are annealed at temperatures between 500 and 700 °C in a $CO / CO_2$ or $H_2 / H_2O$ containing argon carrier gas. The oxygen partial pressure adjusted stepwise between $10^{-23}$ and $10^{-3}$ bar. In order to test the reproducibility, two $p_{O_2}$ ramps are performed for each gas composition and each temperature.

The complex impedance is measured with a Solartron SI1260 gain phase analyzer in a frequency range from 1 Hz to 1 MHz. Subsequently, the impedance spectra are fitted with an electronic circuit consisting of a resistor $R_1$ and a constant phase element CPE connected in parallel, followed by an additional resistor $R_2$ connected in series with the aforementioned $R_1$ | CPE pair. In this model, $R_1$ corresponds to the bulk resistance of the sample and CPE to its capacitive properties, and $R_2$ represents the resistance of the harness.

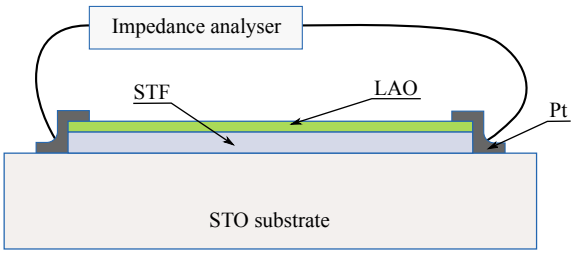


**Figure 6.** Scheme (not to scale) of the electrode arrangement for conductivity measurements. Two wires are attached to the sample using Pt paste at the ends of the rod. Due to the position of the electrodes, the components of the structure are connected in parallel.

The reference sample used for comparison purposes only is a STO substrate without additional layers. Further samples consist of a STO substrate with a 100 nm STF20 and a LAO film on top of it (see Fig 6). Due to the position of the electrodes, the electrical resistance of substrate and films is measured laterally and can be described by resistors connected in parallel. Thus, the total measured conductance $G_{tot}$ is the sum of all contributing conductances,

$$G_{tot} = G_{STO} + G_{STF} + G_{LAO} + G_{iface}. \quad (8)$$

Here, $G_{iface}$ corresponds to the conductance of the interface between STO and STF. The width and length of all layers and the STO substrate are the same. Therefore, the specific conductivity and thicknesses of the layers are relevant parameters only. Since the substrate (500 µm STO) is significantly thicker than the films (e.g., 0.1 µm STF20) or the interface, the specific conductivity of the films or the interface has to be at least several orders of magnitude higher than that of STO to expect a measurable impact on the total measured conductance. Similarly, the capacity of the layers sums up and results in a single measurable element.

## 4 Results and discussion

### 4.1 Pulsed laser deposition

In order to confirm the quality of prepared samples, high-resolution TEM images of the interface are acquired. Here, the specimens are cut into $5 \times 5\,mm^2$ pieces using a diamond saw and processed in a way to obtain a disk with a diameter of about 3 mm and a thickness of 100 µm embedded in an epoxy resin. Subsequently, a dimple is created at the interface zone and, finally, a hole is made using an ion gun.

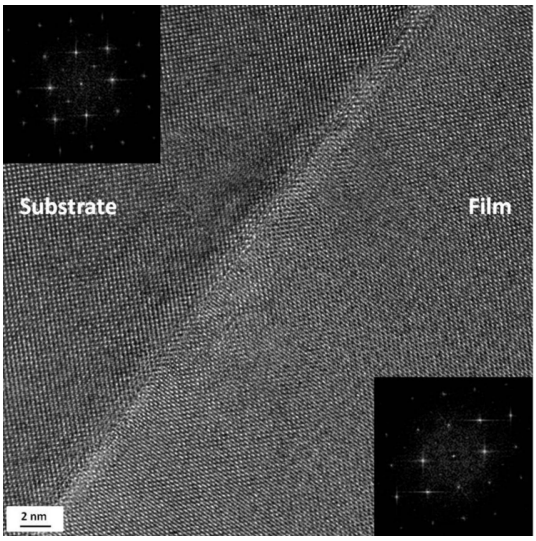


**Figure 7.** High-resolution TEM image of a STF50 | STO interface.

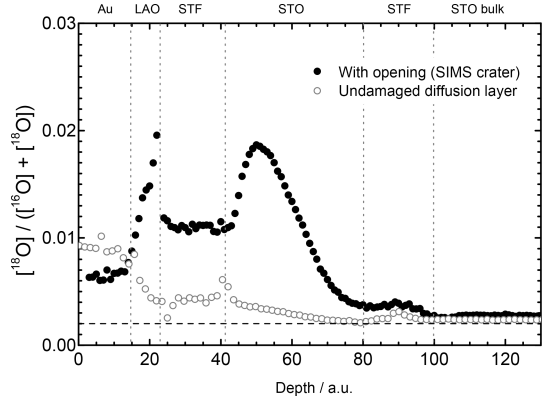


**Figure 8.** Largely suppressed $^{18}O$ concentration in Au | LAO | STF50 | STO | STF50 | STO as a result of an intact Au | LAO diffusion barrier in comparison to the situation with the intentional $^{18}O$ access through the opening (SIMS crater).

A HR-TEM image of the interface between substrate and deposited STF50 (see Fig. 7) confirms epitaxial growth of the layer. The interface is smooth and only a few nanometers thick. The concentration of crystalline defects such as dislocations and grain boundaries appears to be negligible.

## 4.2 Oxygen transport

### 4.2.1 Diffusion barrier

In order to verify the effect of the diffusion barrier, samples with and without the opening (SIMS crater) in the Au | LAO cover layer are annealed in a $^{18}O_2$-enriched atmosphere at 600 °C for 1 h. Subsequently, depth profiles of the $^{18}O$ concentration are acquired. As shown in Fig. 8 the diffusion of oxygen through an undamaged diffusion barrier is largely suppressed.

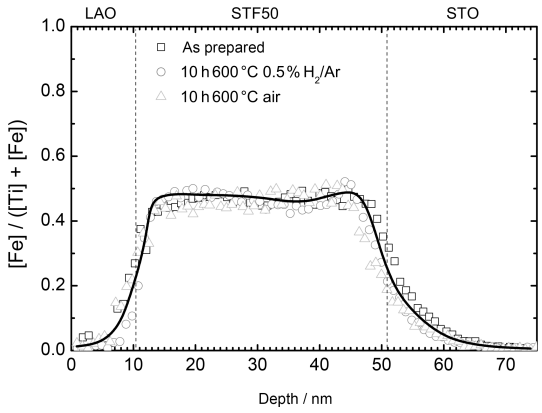


**Figure 9.** Fe profile at the interfaces of a 50 nm thick STF50 sandwiched between LAO and STO before and after 10 h of annealing at 600 °C in air or $H_2$. No measurable change in the profile indicates good thermal stability of nanostructured STO | STF50. The average depth resolution of the measurement is in the range of about 10 nm.

### 4.2.2 Oxygen tracer diffusivity

The second aspect investigated by SIMS is the thermal stability of the thin STF layer as well as the multilayer structures. As shown in Fig. 9, the 10 h annealing at 600 °C does not result in a significant change in the Fe profile compared to the as-prepared sample. There is also no influence of the annealing atmosphere observed. The measured width of the interface is comparable with the one obtained from HR-TEM measurement; however, the thickness cannot be given precisely since the depth resolution of the SIMS workstation is about 10 nm for the given measurement parameters.

The increase in annealing temperature to 700 °C impacts the stability of STF. After an annealing period of 1 h, the width of the interface increases from about 6 to about 14 nm. The width is estimated based on a decrease in the Fe concentration by a factor of $1/e$ (see Fig. 10). Using these data, a chemical diffusion coefficient of Fe is calculated ($D_{Fe} = 2.9 \times 10^{-20}\,m^2\,s^{-1}$; see the dashed line in Fig. 10) using the numeric solution of Fick's second law with the following boundary conditions:

- infinite depth in the direction of the STO substrate;
- a finite Fe source in the form of the STF layer;
- different diffusion coefficients in STF and STO; and
- a ca. 10 nm wide interface area where $D_{Fe}^{STF}$ changes gradually to $D_{Fe}^{STO}$.

The starting point of the simulation is the as-prepared Fe profile in STF and STO.

Although no detailed information regarding the temperature dependence of Fe diffusion is gathered, the activation energy $E_A$ of this process is suspected to be high. Literature data regarding $E_A$ for the Fe diffusion in SFO or STF are

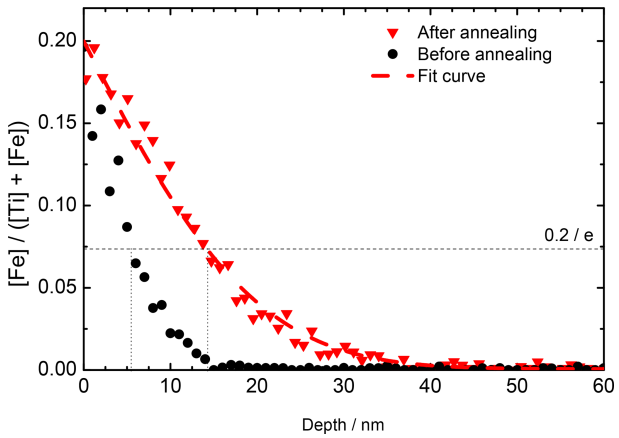


**Figure 10.** The STF20 | STO interface before (black dots) and after 60 min annealing at 700 °C (red triangles). The dashed line represents the result of the numerical diffusion model (see text). The dotted lines correspond to the $1/e$ threshold used to approximate the width of the interface.

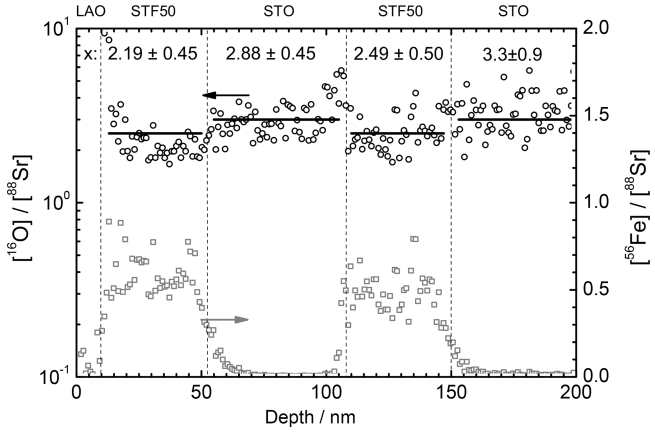


**Figure 11.** Mean oxygen concentration $x$ in LAO | STF50 | STO | STF50 on STO according to the chemical formulas $SrTiO_x$ or $SrTi_{0.5}Fe_{0.5}O_x$. The black lines correspond to $x = 3$ and $x = 2.5$, respectively; the value above the lines is calculated from data points. The iron profile is shown to indicate boundaries (marked by dashed vertical lines) between the STF50 and STO layers. Large noise is caused by a weak and noisy Sr reference signal.

obviously not available. However, the high $E_A$ of 3.3 eV reported for $Ti^{+4}$ ions by Gömann et al. (2004) supports the abovementioned suspicion since $Fe^{+3}$ and $Ti^{+4}$ share a lattice site in STF.

The broadening of the interface limits the long-term application of the structures to about 600–650 °C. It should be avoided to anneal the samples at temperatures exceeding this limit significantly.

An attempt to estimate the mean oxygen concentration $x$ according to chemical formula $SrTi_{1-y}Fe_yO_x$ is shown in Fig. 11. Here, a weak and noisy Sr signal leads to large uncertainties of up to ±0.9 (30 %) in the STO substrate. Therefore, the data are provided for orientation purposes only.

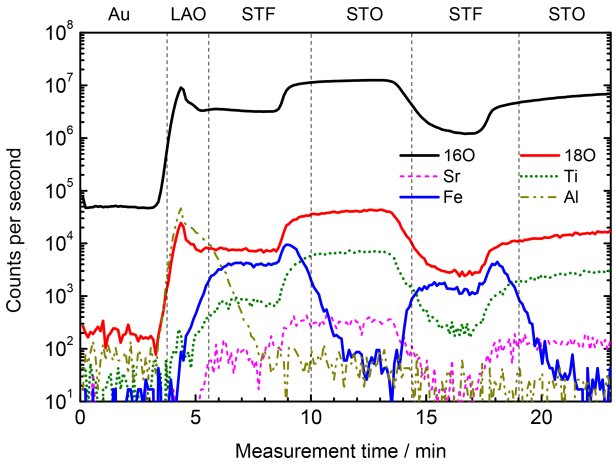


**Figure 12.** Initial SIMS profile of an as-prepared sample with following structure: Au | LAO | STF50 | STO | STF50 on STO. The boundaries of layers are defined as positions, where the concentration of the relevant element, i.e., Fe in STF and Al in LAO, reaches 50 % of the value in the center of the layer.

### 4.3 Oxygen diffusion at the interface

The SIMS measurements prior to annealing of the samples confirm the existence of all layers in the case of single- as well as multi-layer structures. As shown in an exemplary depth profile (see Fig. 12), there are two clearly distinct areas with an enhanced Fe signal which are attributed to STF layers. Between them there is one STO layer. The area close to the surface with an enhanced Al signal is the LAO blocking layer. As the criterion defining the interface between two subsequent layers, a point is chosen at which the concentration of the relevant element falls to 50 % of the value in the center of the layer. It must be noted that the SIMS count rates of both oxygen isotopes in the STF layers are significantly lower than in STO. It may be related to the matrix effect on oxygen ionization probability as well as a slightly different sputter rate in both materials. Moreover, the primary ion beam does not scan the surface only, but also penetrates a few nanometers into the sample. Therefore, the anomalies in the STF layers do not necessarily correspond to the interface. The concentration of $^{18}O$ in the initial profile corresponds to the natural abundance of this isotope of 0.2 %.

#### 4.3.1 Two-dimensional depth profiles

Two-dimensional $^{18}O$ depth profiles measured in STO show a plateau of about 20–30 nm in the vicinity of the STF | STO interface. The plateau is observed not only in the case of annealing at 700 °C, where Fe diffusion into STO was observed, but also for the sample annealed at the significantly

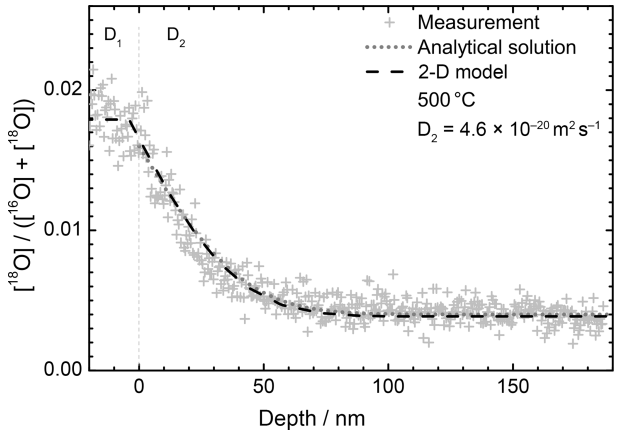


**Figure 13.** Normalized $^{18}O$ depth profile in the vicinity of the STF50 | STO interface obtained after 195 min annealing at 500 °C. Dotted and dashed lines are, respectively, a fit to the analytical solution of Fick's second law and 2-D diffusion simulation with Comsol Multiphysics software. The vertical line separates areas where two different diffusion coefficients, $D_1$ and $D_2$, are applied.

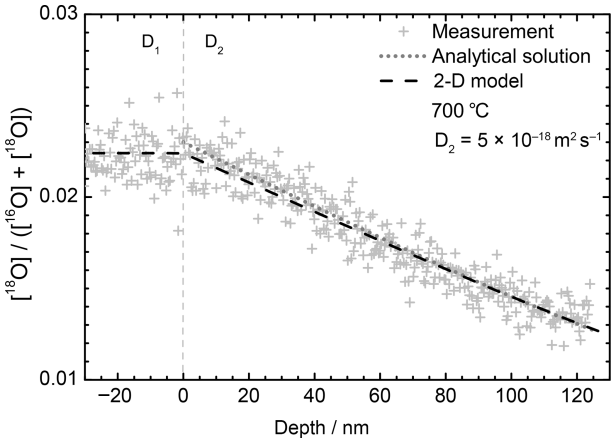


**Figure 14.** Normalized $^{18}O$ depth profile after 60 min annealing at 700 °C.

lower temperature of 500 °C. Therefore, it can be most likely attributed to the space charge zone, where oxygen can quickly diffuse and build a uniform layer. The appearance of the space charge layer is discussed in more detail in Sect. 2.2.5. Once the space charge zone ends, a regular error-function-like profile is observed (see Figs. 13 and 14). In the case of samples annealed at 700 °C, only a portion of the profile in the STO substrate is acquired.

If the plateau is attributed to the space charge zone, its width should be comparable with the Debye length λ:

$$\lambda = \sqrt{\frac{\varepsilon_R \varepsilon_0 k_B T}{4e^2 \left[V_O^{\bullet\bullet}\right]}}, \tag{9}$$

which correlates temperature $T$ and the dielectric constant of STO, $\varepsilon_R$, with the concentration of oxygen vacancies $[V_O^{\bullet\bullet}]$. For example, at a temperature of 700 °C, a Debye length of 30 nm is achieved for an acceptor doping concentration of $[A'] = 7.7 \times 10^{17}\,\mathrm{cm}^{-3}$, which in turn is in the range of an unintended doping.

The diffusion coefficients of oxygen for both temperatures are determined using an analytical solution of Fick's second law, as well as numerically as described in Sect. 2.2.5. The diffusion coefficients $D_2$ for 500 and 700 °C are $4.6 \times 10^{-20}$ and $5 \times 10^{-18}\,\mathrm{m^2\,s^{-1}}$, respectively.

### 4.3.2 Three-dimensional depth profiles

The 3-D analysis of the samples annealed at 600 °C in $^{18}O_2$ shows results dependent on the structure of the samples. In the case of a single STF layer on the STO substrate, a 30 nm thin area with enhanced $^{18}O$ isotope concentration in the STO substrate close to the interface is observed. In the case of structures containing a 50 nm STO film between two 50 nm STF layers, a significantly increased $^{18}O$ concentration in the intermediate STO layer is observed (see Fig. 15). Even larger $^{18}O$ concentrations found in the vicinity of the initial SIMS crater are ignored during data evaluation. Due to a lower yield of secondary ions and a decreased signal-to-noise ratio, the oxygen distribution in the STF layers appears to be spotty. This effect is largely pronounced in the lower STF layer, where the total yield of secondary ions was the lowest.

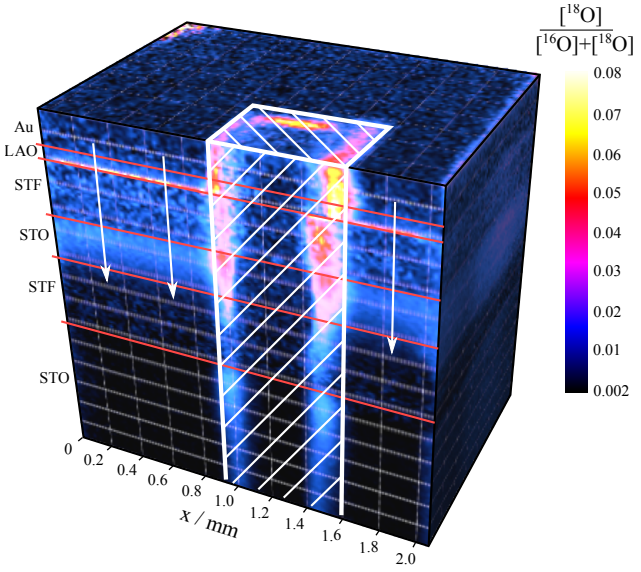


**Figure 15.** Cross section of a 3-D $^{18}O$ profile in the Au | LAO | STF50 | STO | STF50 on STO showing an enhanced oxygen concentration in the intermediate STO layer at 500 °C. The hatched area in the middle of the profile is impacted by the initial SIMS crater and is not used for data evaluation. The arrows indicate the direction of 2-D $^{18}O$ profiles as shown, e.g., in Fig. 4.

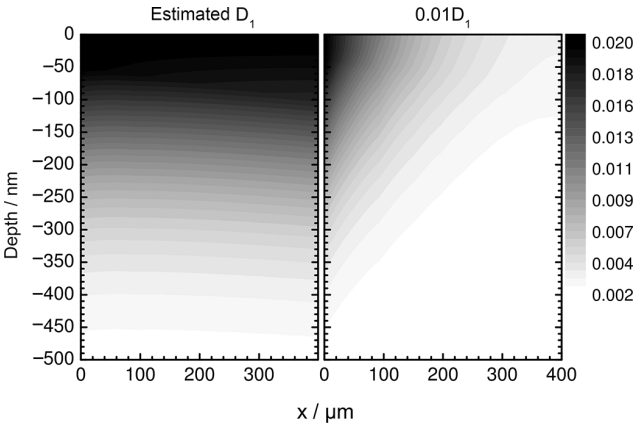


**Figure 16.** Two cross sections of oxygen distribution showing the influence of the oxygen diffusion coefficient at the interface on the shape of the concentration depth profile.

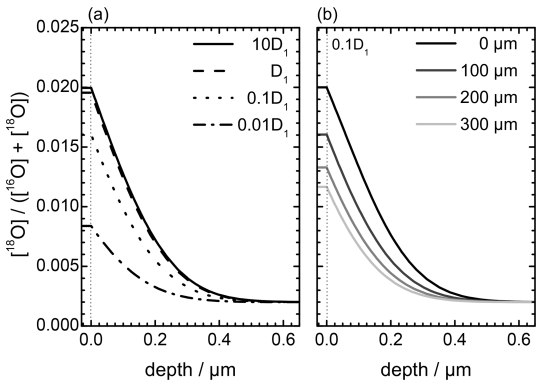


**Figure 17.** Impact of the oxygen diffusion coefficient along the interface on the oxygen depth profile acquired 100 µm from the initial SIMS crater. Higher diffusion coefficients ($D_1$ and $10D_1$ in this example) do not cause any significant change in the profile, whereas lower coefficients ($0.1D_1$ and $0.01D_1$) cause unequal oxygen distribution in the interface area.

Intentionally, the center of the crater sputtered prior to the oxygen exchange experiments just reaches the STO substrate. The latter is used as indicator of a sufficiently deep crater to enable oxygen exchange at the upper STF | STO interface. Obviously, rounded edges at the crater bottom prevent significant $^{18}$O exchange as shown in Fig. 15. The effect might be caused by the distance between the rounded crater surface and that part of the interface between STF and STO substrate evaluated after the $^{18}$O exchange. Further, the formation of space charges might be suppressed in this region. Consequently, there is almost no $^{18}$O visible at the interface of the STF and STO substrate. It should be noted further that Fig. 15 shows an open interface between STF and STO substrate which is, however, created during the second sputter run after the $^{18}$O exchange experiments.

One can observe that $^{18}$O fills the space charge layer almost uniformly over a large area within a relatively short time. This indicates that the oxygen diffusion coefficient at the interface is much larger than in pure STO or STF. Based on the SIMS data, a value of $D_1 = 3.4 \times 10^{-10}\,\mathrm{m^2\,s^{-1}}$ at 600 °C along the interface is found using an analytical solution of Fick's second law.

Since such multilayer stacks might be applied as fast ionic conductors, a comparison of oxygen diffusivity between the STF | STO system and commercially available materials is done. For example, the oxygen diffusion coefficient $D_O$ of the application relevant material YSZ at the same temperature is about 2 to $3 \times 10^{-12}\,\mathrm{m^2\,s^{-1}}$ (Kilo et al., 2004), which is comparable with oxygen diffusion in SFO and STF solid solutions, but approximately 2 orders of magnitude lower than that at the STF | STO interface.

### 4.3.3 Correlation with the numerical model

In order to estimate the range of measurable oxygen diffusion coefficients along the interface, the numerical model of STO described in Sect. 2.2.5 is applied to simulate the 2-D diffusion process in the STO substrate (using the diffusion coefficient $D_2$) and at the interface (using the diffusion coefficient $D_1$).

Simultaneous diffusion of oxygen along the interface and in the bulk requires the consideration of two different experimental aspects. First, for a given temperature, the annealing time has to be large enough to enable oxygen diffusion in the bulk. An underestimated time results in a natural abundance of the tracer measured through the entire sample. On the other hand, the overestimated annealing time results in a sample saturated with the $^{18}$O tracer where the impact of the interface on the diffusion profile is not visible anymore. The second aspect depends on the ratio of both oxygen diffusion coefficients, $D_1$ and $D_2$. If the ratio is not large enough, a non-symmetrical diffusion profile, as shown in the right part of Fig. 16, is expected.

Since the 3-D SIMS measurement revealed a uniform distribution of $^{18}$O along the entire interface, it is assumed that the diffusion coefficient $D_1$ must be sufficiently high to provide identical depth profiles calculated for different distances from the opening in the diffusion barrier (see the vertical arrows in Fig. 4). Choosing a sufficiently high $D_1$, the simulated 2-D oxygen-18 concentration profile exhibits uniform distribution in the $x$ direction, as shown in the left part of Fig. 16. An equivalent statement concerns the line scans at different distances from the initial SIMS crater. They are similar, which corresponds to the experimental findings. Further, the diffusion coefficient at the interface and in bulk STO should enable one to fit the $^{18}$O depth profiles (see Figs. 13 and 14).

It must be noted that this approach allows one only to determine the lowest possible limit for $D_1$ and does not result in exact values. As shown in Fig. 17 the simulation results obtained for $D_1$ and $10D_1$ are practically the same.

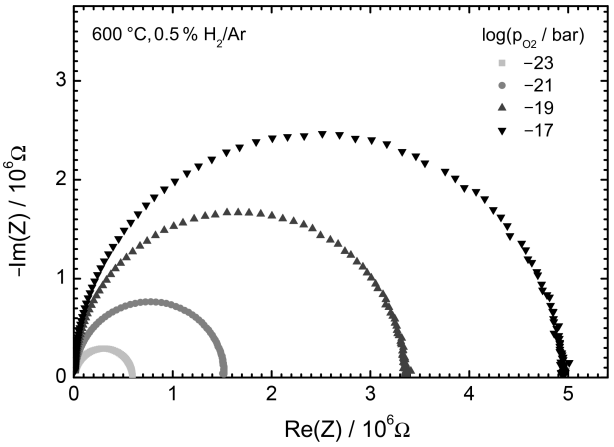


**Figure 18.** Exemplary Nyquist plot of STF20 on STO impedance measured at 600 °C at four different oxygen partial pressures. The resistance determining the diameter of the semicircle is discussed at the end of Sect. 4.4.1.

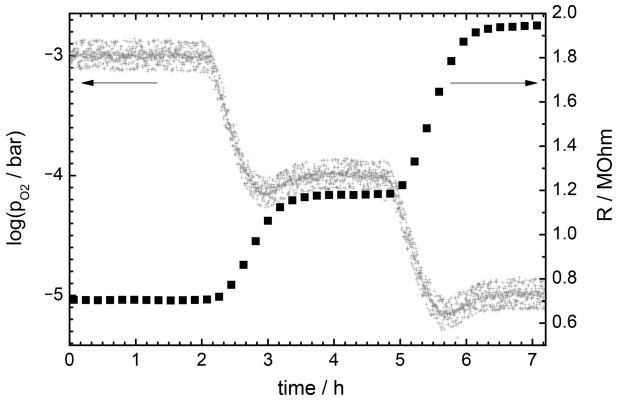


**Figure 19.** Exemplary plot showing the change in the resistance of STF20 on the STO sample (see Sect. 3.4) during changes in the oxygen partial pressure. Large $p_{O_2}$ noise is caused by operating the oxygen sensor at the low temperature of 500 °C.

The numerical approach not only enabled simulation on the entire oxygen concentration profile, including the STO | STF interface and the STO substrate, as shown in the form of the dashed line in Figs. 13 and 14, but also enabled one to estimate a lowest limit for the oxygen diffusion coefficient of $3 \times 10^{-10}$ m$^2$ s$^{-1}$ at 500 °C and of $10^{-9}$ m$^2$ s$^{-1}$ at 700 °C.

### 4.4 Oxygen partial pressure-dependent conductivity

The measured impedance spectra as shown in Fig. 18 yield well-shaped semicircles with $p_{O_2}$ and a $T$-dependent diameter. As already mentioned in Sect. 3.4, only one single semicircle, with the lowest resistance and the highest capacitance dominating, is obtained due to the parallel arrangement of resistors and capacities for STF, STO and the interface. Fitting the spectra with the electrical equivalent circuit mentioned in Sect. 3.4 allows one to determine the bulk conductivity $R_1$. The resistance $R_2$ related to the harness is negligibly low. The phase of the CPE is very close to the unity.

The determination of the conductivity is performed in two different gas buffer compositions, CO / $CO_2$ and $H_2$ / $H_2O$. Both gas mixtures are applied to figure out whether the conductivity is affected by, e.g., diffusion of hydrogen or hydroxyl groups in STO crystals as described by Steinsvik et al. (2001).

After the set temperature stabilizes, the $p_{O_2}$ is firstly decreased stepwise from $10^{-3}$ to $10^{-23}$ bar and then increased stepwise back to $10^{-3}$ bar. At each step, the oxygen partial pressure is held constant until the measured impedance stabilizes. The criteria are changes in the measured resistance below 1 %. After a complete $p_{O_2}$ loop, the next temperature is adjusted. This process is shown exemplarily in Fig. 19, where the changes in oxygen partial pressure and sample resistance are shown as a function of time.

**Table 1.** Minimum of electronic conductivity, ionic conductivity and oxygen partial pressure at the intrinsic point obtained from the fit of Eq. (10).

| $T$ (°C) | Buffer | $\sigma_{el,min}$ (S m$^{-1}$) | $\sigma_{ion}$ (S m$^{-1}$) | $\log(p^*_{O_2})$ (bar) |
|---|---|---|---|---|
| 510 | $H_2$ / $H_2O$ | $6.5 \times 10^{-6}$ | $5.9 \times 10^{-4}$ | – |
| 510 | CO / $CO_2$ | $9.3 \times 10^{-7}$ | $4.8 \times 10^{-4}$ | – |
| 600 | $H_2$ / $H_2O$ | $6.5 \times 10^{-5}$ | $1.3 \times 10^{-3}$ | −13.6 |
| 600 | CO / $CO_2$ | $4.1 \times 10^{-5}$ | $1.1 \times 10^{-3}$ | −14.6 |
| 690 | $H_2$ / $H_2O$ | $5.1 \times 10^{-4}$ | $2.6 \times 10^{-3}$ | −11.0 |
| 690 | CO / $CO_2$ | $5.4 \times 10^{-4}$ | $2.6 \times 10^{-3}$ | −11.1 |

The total conductivity plotted against oxygen partial pressure shows a shape typical of the predominant $n$ type electronic conductivity at low oxygen partial pressures, ionic conductivity at intermediate $p_{O_2}$ and $p$ type electronic conductivity at high oxygen partial pressures. The $-1/4$ and $+1/4$ slopes of $n$ and $p$ type electronic conductivities indicate that the oxygen vacancy concentration is independent of the oxygen partial pressure. Here, the experimental data are fitted using the formula given by, e.g., Yoo et al. (2002):

$$\sigma = \sigma_{el,min} \times \cosh\left[\frac{1}{4}\ln\left(\frac{p_{O_2}}{p^*_{O_2}}\right)\right] + \sigma_{ion}, \quad (10)$$

where the minimum of electronic conductivity is given by $\sigma_{el,min} = 2q(\mu_n\mu_p)^{1/2}n_i$. Further, $\mu_n$ and $\mu_p$ are electron and hole mobilities, $n_i$ is the charge carrier concentration, $p^*_{O_2} = (\mu_n/\mu_p)^2 p^0_{O_2}$ and $p^0_{O_2}$ is the oxygen partial pressure at the intrinsic point, i.e., when $n = p = n_i$. The equation is fitted to each measured data set (different $p_{O_2}$ at constant temperature and gas composition) with $\sigma_{ion}$, $\sigma_{el,min}$ and $p^*_{O_2}$ fitting parameters.

Using Eq. (10) the ionic conductivity $\sigma_{ion}$ is separated from the total conductivity $\sigma$. Further, the temperature

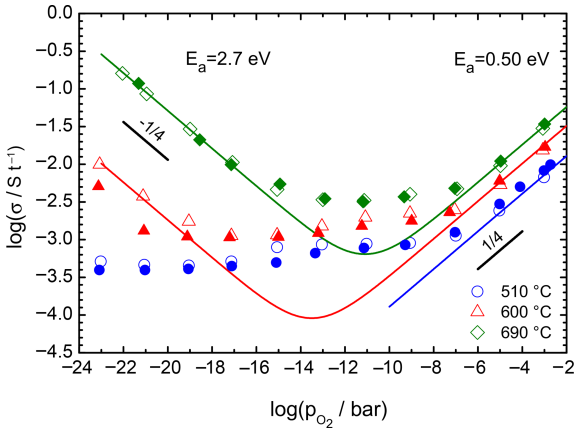


**Figure 20.** Total electrical conductivity of the STF20 layer on the STO substrate as a function of oxygen partial pressure and temperature. The measurements are performed in $CO / CO_2$ (closed symbols) and $H_2 / H_2O$ (open symbols) containing atmospheres.

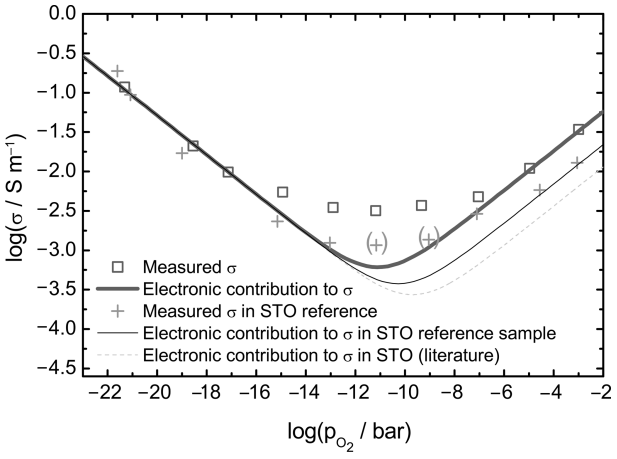


**Figure 21.** Total electrical conductivity of the STF20 | STO system (squares) and STO reference sample (plus sign) as well as electronic conductivity of the STF20 | STO system (thick line), STO reference sample (line) and STO following Ohly et al. (2006) (dashed line) at 690 °C.

dependence of the minimum of electronic conductivity, $\sigma_{el,min} = \sigma_0 \exp(-E_g/2kT)$, enables one to extract the band-gap energy $E_g$.

The results show that there is only a slight difference in the conductivity measured in two different gas mixtures (see Table 1). In the case of the carbon monoxide containing atmosphere, the $n$ type conductivity at low oxygen partial pressures is slightly lower compared to the hydrogen containing atmosphere. One can recognize three regions in the conductivity data:

- $n$ type conductivity below $10^{-16}$ bar with $\sigma \propto p_{O_2}^{-1/4}$ and $E_A = 3.4$ eV (CO)/2.7 eV ($H_2$);
- ionic conductivity in the intermediate range with $E_A =$ 0.7 eV (CO)/0.6 eV ($H_2$);
- $p$ type conductivity above $10^{-9}$ bar with $\sigma \propto p_{O_2}^{1/4}$ and $E_A = 0.46$ eV (CO)/0.50 eV ($H_2$).

The activation energies for $p$ and $n$ type electronic conductivity are found to be lower than those of pure STO crystals. Balachandran and Eror (1981) report activities of, respectively, 1.56 and 4.56 eV; Chan et al. (1981) report activation energy of $p$ type conductivity of 0.98 eV. The activation energy of ionic conductivity and thus of oxygen vacancy diffusion is lower than the 0.99 eV measured in pure STO by Ohly et al. (2006).

The band-gap enthalpy $E_g$ determined from the intrinsic minima of the electronic conductivity ($\sigma_n + \sigma_p$) is found to be 3.2 eV. The value is in good agreement with band-gap enthalpies reported by other authors (3.36 eV – Balachandran and Eror, 1981; 3.30 eV – Chan et al., 1981; 3.30 eV – Ohly et al., 2006; 3.2 eV – Rothschild, 2006).

The measurement in hydrogen and carbon monoxide containing atmospheres is shown in Fig. 20. Here, the modeled $n$ type conductivity contribution at 510 °C does not exceed the ionic conductivity and is, therefore, not shown.

### 4.4.1 Conductivity comparison with pure STO

At oxygen partial pressures below $10^{-15}$ bar the predominant $n$ type conductivity of the STF20 | STO sample is exactly the same as in the case of pure STO. At intermediate oxygen partial pressures between $10^{-15}$ and $10^{-7}$ bar an increase in ionic conductivity is observed. Similarly, at $p_{O_2}$ above $10^{-7}$ bar an increase in the predominant $p$ type conductivity is measured.

At an oxygen partial pressure of 1 mbar and a temperature of 690 °C the total sample resistance is 157.4 kΩ, which corresponds to a total conductivity of $3.4 \times 10^{-2}$ S m$^{-1}$ . The resistance expected for STO at the same conditions (geometry, temperature and $p_{O_2}$) is, however, significantly higher and equals 460.3 kΩ, corresponding to $1.2 \times 10^{-2}$ S m$^{-1}$. One of the reasons could be the contribution to the conductivity from the STF20 layer. However, having its thickness of 100 nm in mind, its resistance would be about 5.1 GΩ even though the specific conductivity of 5.2 S m$^{-1}$ is much higher than that of STO. Even if one considers Fe diffusion from STF20 into STO and, as a worst-case scenario, the width of the STF layer increase from 100 to 130 nm, the contribution from STF alone is not sufficient to explain the high conductivity.

Another explanation of conductivity enhancement is the contribution of the space charge zone. In order to match the resistance of the measured sample with the resistance of STO and resistance of STF20, one would require an additional element with $R = 250.7$ kΩ. Using the thickness of all layers, the conductivity in the space charge zone can be calculated. At 700 °C and with a given zone width of 30 nm, one calculates the conductivity at the interface to be about 360 S m$^{-1}$.

In this calculation the STF20 conductivity is taken from Moos et al. (2000). The resistance of the space charge zone (250.7 kΩ) is considerably lower than the resistance of STO bulk (460.3 kΩ) and as such contributes significantly to the total resistance of the sample. Therefore, the diameter of the semicircles shown in Fig. 18 is largely determined by the transport in the space charge zone.

#### 4.4.2 Linking the diffusion data with ionic conductivity

Assuming that the ionic contribution in STF20 films on STO is attributed to Frenkel defects, the oxygen diffusion coefficient can be calculated from the conductivity data. The 3-D SIMS measurements reveal a 30 nm thick layer of enhanced oxygen diffusivity in STO in the vicinity of the interface. Using this number and the ionic contribution to $\sigma$, an oxygen diffusion coefficient of $D_O = 2.0 \times 10^{-10}\,m^2\,s^{-1}$ is obtained. Having the uncertainty of the measurements in mind, the value is in good agreement with the fit of oxygen concentration obtained by SIMS measurements at the same temperature ($3.4 \times 10^{-10}\,m^2\,s^{-1}$ at 600 °C). For comparison, oxygen diffusivity in nominally undoped STO is lower by several orders of magnitude, i.e., about $10^{-15}\,m^2\,s^{-1}$ at 600 °C as reported by Paladino et al. (1965).

## 5 Conclusions

Epitaxial structures containing interleaved STO and STF layers grown epitaxially on STO substrates are investigated by oxygen tracer diffusion experiments and impedance spectroscopy at different temperatures and oxygen partial pressures. Three-dimensional element profiles show increased $^{18}O$ concentration in the vicinity of the interface (thickness: 30 nm) between STF and STO, which in turn confirms that the oxygen diffusion coefficient in that area increases significantly. A numerical model limits possible diffusion coefficients along the interface to a minimum value. The lowest possible $D_1$ leading to uniform oxygen-18 concentration profiles is $3 \times 10^{-10}\,m^2\,s^{-1}$ at 500 °C, which is a few orders of magnitude higher than the diffusion coefficient of oxygen in bulk STO, $D_2$.

Conductivity measurements in $H_2$ / $H_2O$ and CO / $CO_2$ show that there is only minor impact of the atmosphere on the resistance of the structures. The materials show a slightly increased $p$ type and ionic conductivity in comparison to pure STO. The oxygen diffusion coefficient calculated from the conductivity data shows good agreement with that of SIMS measurements.

**Competing interests.** The authors declare that they have no conflict of interest.

**Acknowledgements.** This joint research project was financially supported by the state of Lower Saxony and the Volkswagen Foundation, Hannover, Germany.

Edited by: J. Zosel
Reviewed by: two anonymous referees

## References

Badwal, S.: Zirconia-based solid electrolytes: microstructure, stability and ionic conductivity, Solid State Ionics, 52, 23–32, 1992.

Balachandran, U. and Eror, N.: Electrical Conductivity in Strontium Titanate, J. Solid State Chem., 39, 351–359, 1981.

Chan, N.-H., Sharma, R., and Smyth, D.: Nanostoichiometry in $SrTiO_3$, J. Electrochem. Soc., 128, 1762–1768, 1981.

Comsol: COMSOL Multiphysics, COMSOL Multiphysics 5.1, https://www.comsol.de/comsol-multiphysics (last access: 14 April 2015), 2016.

De Souza, R.: The formation of equilibrium space-charge zones at grain boundaries in the perovskite oxide $SrTiO_3$, Phys. Chem. Chem. Phys., 11, 9939–9969, 2009.

De Souza, R.: Oxygen Diffusion in $SrTiO_3$ and Related Perovskite Oxides, Adv. Funct. Mater., 25, 6326–6342, 2015.

Fergus, J. W.: Perovskite oxides for semiconductor-based gas sensors, Sensor. Actuat. B-Chem., 123, 1169–1179, 2007.

Gerstl, M., Frömling, T., Schintlmeister, A., Hutter, H., and Fleig, J.: Measurement of $^{18}O$ tracer diffusion coefficients in thin yttria stabilized zirconia films, Solid State Ionics, 184, 23–26, 2011.

Gömann, K., Borchardt, G., Gunhold, A., Maus-Friedrichs, W., and Baumann, H.: Ti diffusion in La-doped $SrTiO_3$ single crystals, Phys. Chem. Chem. Phys., 6, 3639–3644, 2004.

Gömann, K., Borchardt, G., Schulz, M., Gömann, A., Maus-Friedrichs, W., Lesage, B., Kaïtasov, O., Hoffman-Eifert, S., and Schneller, T.: Sr diffusion in undoped and La-doped $SrTiO_3$ single crystals under oxidizing conditions, Phys. Chem. Chem. Phys., 7, 2053–2060, 2005.

Heilig, C.: Characterisierung der elekrischen Eigenschaften von $Sr(Ti,Fe)O_3$ im Hinblick auf die Anwendung in Sauerstoffsensoren (Characterization of the Electrical Properties of $Sr(Ti,Fe)O_3$ in View of an Application as Oxygen Sensors), Diploma Thesis (in German), Universität Karlsruhe (TH), Karlsruhe, Germany, 1996.

Hu, Y., Tan, O., Cao, W., and Zhu, W.: A low temperature nanostructured $SrTiO_3$ thick film oxygen gas sensor, Ceramics International, 30, 1819–1822, doi:10.1016/j.ceramint.2003.12.068, 2004.

Ioffe, A., Rutman, D., and Karpachov, S.: On the nature of the conductivity maximum in zirconia-based solid electrolytes, Electrochemica Acta, 23, 141–142, 1978.

Kilo, M., Argirusis, C., Borchardt, G., and Jackson, R.: Oxygen diffusion in yttria stabilised zirconia – experimental results and molecular dynamics calculations, Phys. Chem. Chem. Phys., 5, 2219–2224, 2004.

Kozhevnikov, V. L., Leonidov, I. A., Patrakeev, M. V., Mitberg, E. B., and Poeppelmeier, K. R.: Electrical Properties of the Ferrite $SrFeO_y$ at High Temperatures, J. Solid State Chem., 158, 320–326, 2001.

Kuhn, M., Kim, J. J., Bishop, S. R., and Tuller, H. L.: Oxygen Nonstoichiometry and Defect Chemistry of Perovskite-Structured

$Ba_xSr_{1-x}Ti_{1-y}Fe_yO_{3-y/2+\delta}$ Solid Solutions, Chem. Mater., 25, 2970–2975, 2013.

Metlenko, V., Ramadan, A. H. H., Gunkel, F., Du, H., Schraknepper, H., Hoffmann-Eifert, S., Dittmann, R., Waser, R., and De Souza, R. A.: Do dislocations act as atomic autobahns for oxygen in the perovskite oxide $SrTiO_3$?, Nanoscale, 6, 12864–12876, doi:10.1039/C4NR04083J, 2014.

Moos, R., Menesklou, W., Schreiner, H.-J., and Härdtl, K. H.: Materials for temperature independent resistive oxygen sensors for combustion exhaust gas control, Sensor. Actuat. B-Chem., 67, 178–183, 2000.

Ohly, C., Hoffmann-Eifert, S., Guo, X., Schubert, J., and Waser, R.: Electrical Conductivity of Epitaxial $SrTiO_3$ Thin Films as a Function of Oxygen Partial Pressure and Temperature, J. Am. Ceram. Soc., 89, 2845–2852, 2006.

Paladino, A. E., Rubin, L. G., and Waugh, J. S.: Oxygen ion diffusion in single crystal $SrTiO_3$, J. Phys. Chem. Solids, 26, 391–397, 1965.

Rothschild, A.: Electronic Structure, Defect Chemistry, and Transport Properties of $SrTi_{1-x}Fe_xO_{3-y}$ Solid Solutions, Chem. Mater., 18, 3651–3659, 2006.

Schulz, M., Brillo, J., Stenzel, C., and Fritze, H.: Oxygen partial pressure control for microgravity experiments, Solid State Ionics, 225, 332–336, doi:10.1016/j.ssi.2012.04.008, 2012.

Shi, T., Chen, Y., and Guo, X.: Defect chemistry of alkaline earth metal (Sr/Ba) titanates, Prog. Mater. Sci., 80, 77–132, 2016.

Steinsvik, S., Bugge, R., Gønnes, J., Taftø, J., and Norby, T.: The defect structure of $SrTi_{1-x}Fe_xO_{3-y}$ ($x = 0 - 0.8$) investigated by electrical conductivity measurements and electron energy loss spectroscopy (EELS), J. Phys. Chem Solids, 6, 969–976, 1996.

Steinsvik, S., Larring, Y. J., and Norby, T.: Hydrogen ion conduction in iron-substituted strontium titanate, $SrTi_{1-x}Fe_xO_{3-x/2}$ ($0 \leq x \leq 0.8$), Solid State Ionics, 143, 103–116, 2001.

Wagner, S., Menesklou, W., Schneider, T., and Ivers-Tiffee, E.: Kinetics of oxygen incorporation into $SrTiO_3$ investigated by frequency-domain analysis, J. Electroceram., 13, 645–651, doi:10.1007/s10832-004-5171-2, 2004.

Yoo, H.-I., Song, C.-R., and Lee, D.-K.: $BaTiO_{3-\delta}$: Defect Structure, Electrical Conductivity, Chemical Diffusivity, Thermoelectric Power, and Oxygen Nonstoichiometry, J. Electroceram., 8, 5–36, 2002.